

Pore Environment Effects on Catalytic Cyclohexane Oxidation in Expanded Fe₂(dobdc) Analogues

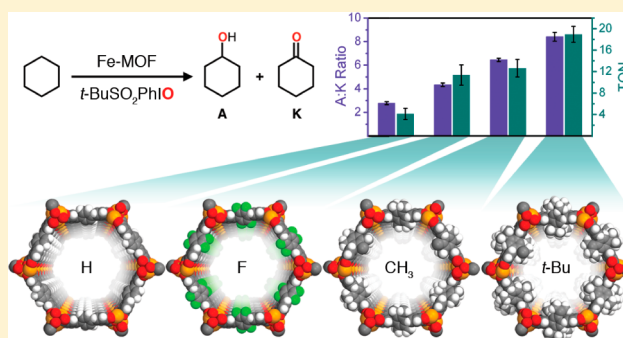
Dianne J. Xiao,[†] Julia Oktawiec,[†] Phillip J. Milner,[†] and Jeffrey R. Long^{*,†,‡,§}

[†]Department of Chemistry and [‡]Department of Chemical and Biomolecular Engineering, University of California, Berkeley, California 94720, United States

[§]Materials Sciences Division, Lawrence Berkeley National Laboratory, Berkeley, California 94720, United States

S Supporting Information

ABSTRACT: Metal–organic frameworks are a new class of heterogeneous catalysts in which molecular-level control over both the immediate and long-range chemical environment surrounding a catalytic center can be readily achieved. Here, the oxidation of cyclohexane to cyclohexanol and cyclohexanone is used as a model reaction to investigate the effect of a hydrophobic pore environment on product selectivity and catalyst stability in a series of iron-based frameworks. Specifically, expanded analogues of Fe₂(dobdc) (dobdc⁴⁻ = 2,5-dioxido-1,4-benzenedicarboxylate) were synthesized and evaluated, including the biphenyl derivative Fe₂(dobpdc) (H₄dobpdc = 4,4'-dihydroxy-[1,1'-biphenyl]-3,3'-dicarboxylic acid), the terphenyl derivative Fe₂(dotpdc) (H₄dotpdc = 4,4''-dihydroxy-[1,1':4',1''-terphenyl]-3,3''-dicarboxylic acid), and three modified terphenyl derivatives in which the central ring is replaced with tetrafluoro-, tetramethyl-, or di-*tert*-butylaryl groups. Within these five materials, a remarkable 3-fold enhancement of the alcohol:ketone (A:K) ratio and an order of magnitude increase in turnover number are achieved by simply altering the framework pore diameter and installing nonpolar functional groups near the iron site. Mössbauer spectroscopy, kinetic isotope effect, and gas adsorption measurements reveal that variations in the A:K selectivities arise from differences in the cyclohexane adsorption enthalpies of these frameworks, which become more favorable as the number of hydrophobic residues and thus van der Waals interactions increase.



INTRODUCTION

The strategic placement of noncovalent interactions around a catalytic center can lead to marked increases in selectivity, activity, and stability. First discovered in enzymes, this principle has been subsequently explored in a wide range of molecular, supramolecular, and heterogeneous systems.¹ Accordingly, bioinspired design elements such as distal hydrogen bond donors,² hydrophobic binding cavities,³ and confined environments^{4,5} have been incorporated into catalysts for natural product synthesis,⁶ small molecule activation,^{7–9} and hydrocarbon cracking.¹⁰ While these examples highlight the importance of functional outer coordination spheres in metal-mediated reactions, precise control over the periphery of an active site remains synthetically challenging in nonbiological systems. Often, the most readily modifiable peripheral parameter is the reaction medium, which has been shown to play a significant role in determining reaction outcomes.¹¹ In zeolites, an additional set of tunable parameters includes the physical dimensions and geometries of the pores, leading to size- and shape-selective catalysis.^{12,13} The hydrophobicity of zeolites can also be controlled by varying the Si/Al ratio and number of hydroxyl defects, guiding selectivity in cases where reactants or products possess large polarity differences.¹³

However, the small pores of zeolites, typically less than 1 nm in diameter,¹⁴ restrict further functionalization of the interior surface. Ordered mesoporous silicates possess larger pores and hydroxyl moieties that can be postsynthetically modified, but their surfaces are locally inhomogeneous and poorly defined.¹⁵

Metal–organic frameworks, a class of highly crystalline solids displaying microporosity and in some cases mesoporosity, are an intriguing platform for systematically evaluating the effects of pore size, shape, and chemical environment on the behavior of a supported catalyst. Tailored pore environments that maximize favorable noncovalent interactions between the framework surface and specific guest molecules can be readily engineered, and are routinely exploited for selective gas separation and storage applications.¹⁶ Highly complex pore interiors containing multiple functional groups in crystallographically or spectroscopically well-defined arrangements have been achieved in certain structure types.¹⁷ In addition to coordinatively unsaturated metal nodes, a variety of organic, organometallic, and nanoparticle moieties can be installed within metal–organic frameworks,^{18,19} forming structurally

Received: August 11, 2016

Published: October 5, 2016

well-defined active sites that, in certain cases, can even be characterized by single crystal X-ray diffraction.²⁰ Taken together, these findings suggest that the nature of a catalytic center and its spatial organization, the identity and placement of surrounding surface functionalities, and the overall pore architecture can all be manipulated with angstrom-level precision in a metal–organic framework.

A common outer coordination sphere motif in metalloenzymes, particularly in the context of hydrocarbon oxidation and metal–oxo chemistry, is the presence of a hydrophobic binding pocket near the transition-metal active site.^{1,21} In the field of homogeneous supramolecular catalysis, cyclodextrins, cyclophanes, and other container-shaped molecules have all been investigated as model substrate binding pockets.³ These hydrophobic cavities shelter reactive intermediates from unwanted side reactions, enhance reaction rates due to favorable substrate binding properties, and guide regio- and stereoselectivity when complex organic substrates are introduced.^{1,3,22} Furthermore, by selectively increasing the local concentration of a substrate, hydrophobic cavities can also minimize undesirable overoxidation processes.¹³ It is anticipated that many of these attractive bioinspired features can be replicated and even expanded upon in metal–organic frameworks featuring exposed redox-active transition metal sites and modifiable pore walls.

Herein, the effects of a local hydrophobic environment on product selectivity and catalyst stability are investigated with respect to cyclohexane oxidation in expanded analogues of Fe₂(dobdc) (dobdc⁴⁻ = 2,5-dioxido-1,4-benzenedicarboxylate), a metal–organic framework featuring exposed iron(II) sites. A 3-fold enhancement of the alcohol:ketone (A:K) product ratio and an order of magnitude increase in turnover number can be achieved by simply altering the framework pore diameter and installing nonpolar, hydrophobic functional groups near the iron center. Detailed Mössbauer spectroscopy, kinetic isotope effect, and adsorption studies suggest that the selectivity enhancement is due to the ability of the hydrophobic functional groups to increase the local concentration of cyclohexane near the reactive iron–oxo intermediate.

EXPERIMENTAL SECTION

Framework Syntheses. In an N₂-filled glovebox, H₄(dotpdc) (60 mg, 0.17 mmol, 1.0 equiv), FeCl₂ (60 mg, 0.47 mmol, 2.8 equiv), DMF (8.0 mL), and MeOH (1.0 mL) were combined in a 20 mL scintillation flask. The vial was sealed with a Teflon-lined cap and heated to 140 °C for 2 days. The resulting precipitate was filtered, washed with DMF (3 × 10 mL at 120 °C) and MeOH (3 × 10 mL at 60 °C), and dried under vacuum at 120 °C for 2 h. To exchange the bound methanol molecules for CD₃CN, the powder was immersed in 0.5 mL of CD₃CN and exposed to a vacuum at 120 °C for another 2 h, affording 66 mg (70%) of Fe₂(dotpdc)·2CD₃CN as a yellow-green powder. The compounds Fe₂(dotpdc^F)·2CD₃CN, Fe₂(dotpdc^{CH₃})·2CD₃CN, and Fe₂(dotpdc^{tBu})·2CD₃CN were synthesized in a similar manner. Anal. Calcd for C₂₄H₁₀D₆Fe₂N₂O₆: C, 52.78; H, 2.95; N, 5.13. Found: C, 52.69; H, 2.55; N, 4.60. IR (solid-ATR): 1615(s), 1553(s), 1541(s), 1519(s), 1466(s), 1432(s), 1399(s), 1380(m), 1303(s), 1235(s), 1146(s), 1104(m), 1052(m), 900(m), 821(s), 724(s), 657(s), 612(s), 580(m).

Yield of Fe₂(dotpdc^F)·2CD₃CN: 50 mg, 57% yield. Anal. Calcd for C₂₄H₆D₆F₄Fe₂N₂O₆: C, 46.64; H, 1.96; N, 4.53. Found: C, 46.33; H, 1.54; N, 4.25. IR (solid-ATR): 1616(s), 1558(s), 1554(s), 1506(m), 1481(s), 1456(s), 1421(s), 1381(s), 1304(s), 1247(s), 1160(s), 1095(s), 978(s), 922(m), 845(s), 832(s), 809(s), 700(s), 659(s), 632(s), 605(m).

Yield of Fe₂(dotpdc^{CH₃})·2CD₃CN: 55 mg, 62% yield. Anal. Calcd for C₂₈H₁₈D₆Fe₂N₂O₆: C, 55.84; H, 4.02; N, 4.65. Found: C, 55.94; H, 4.17; N, 4.30. IR (solid-ATR): 1614(s), 1552(s), 1534(s), 1489(s), 1462(w), 1425(s), 1408(s), 1375(s), 1296(s), 1235(s), 1156(m), 1126(w), 1097(m), 1010(m), 909(w), 859(m), 829(s), 807(m), 756(s), 702(m), 654(s), 628(s), 603(s), 584(m).

Yield of Fe₂(dotpdc^{tBu})·2CD₃CN: 60 mg, 70% yield. Anal. Calcd for C₃₂H₂₆D₆Fe₂N₂O₆: C, 58.38; H, 4.90; N, 4.26. Found: C, 58.43; H, 5.45; N, 4.16. IR (solid-ATR): 1614(s), 1552(s), 1533, 1471, 1422, 1393(w), 1377(s), 1362(s), 1295(s), 1237(s), 1147(s), 1132(m), 1101(m), 907(m), 846(m), 837(m), 823(m), 748(s), 704(s), 660(s), 634(s), 610(s), 520(s).

Catalytic Cyclohexane Oxidation Procedure. General catalytic conditions to determine A:K ratios are as follows: cyclohexane (0.30 mL, 2.8 mmol) and CD₃CN (1.0 mL) were added to a 20 mL scintillation vial containing 5.0 mg of framework (acetonitrile-solvated form, Fe₂(dotpdc^R)·2CD₃CN). In a separate vial, 25 mg of *t*-BuSO₂PhIO (0.073 mmol) was combined with 1.0 mL of CD₃CN to form a partially dissolved slurry. This slurry was added to the framework and the combined reaction was stirred vigorously at room temperature. After 1.5 h, the reaction was stopped, the framework was removed by filtration, and the products were analyzed by ¹H NMR spectroscopy using 1,4-dichlorobenzene as an internal standard. To determine maximum turnover numbers, the same conditions were used, but with 2.5 mg of framework and slightly larger quantities of oxidant (25–75 mg). Each reaction was run in triplicate to obtain standard deviations. The overall yields (A + 2K, where A and K are cyclohexanol and cyclohexanone, respectively) were calculated based on the amount of oxidant consumed.

Solution-Phase Cyclohexane Adsorption Studies. In a 20 mL scintillation vial, 25 mg of Fe₂(dotpdc^R)·2CD₃CN was immersed in 1.0 mL of a 1 M solution of cyclohexane in acetonitrile. The framework and solution were allowed to sit at room temperature for 4 h, after which a small aliquot of the supernatant was removed and filtered to remove framework particles. The concentration of cyclohexane and acetonitrile in this aliquot was analyzed by gas chromatography using 1,4-dichlorobenzene as an internal standard. Each experiment was run in triplicate. The cyclohexane adsorption capacity (mol/mol framework) was determined according to eq 1,²³ where q_t is the amount of cyclohexane adsorbed at time t (mol/mol framework), C_i is the initial concentration of the adsorbate (mol/L), C_f is the final concentration after adsorption (mol/L), V is the volume of solution initially added to the framework (L), and m is the amount of adsorbent added (mol).

$$q_t = \frac{(C_i - C_f)V}{m} \quad (1)$$

Gas-Phase Cyclohexane Adsorption Studies. For all gas adsorption measurements, 50–100 mg of Fe₂(dotpdc^R)·2DMF was transferred to a preweighed glass sample tube under an atmosphere of nitrogen and capped with a Transeal. Samples were then transferred to a Micromeritics ASAP 2020 gas adsorption analyzer and heated under dynamic vacuum at 140 °C until the outgas rate at the degassing temperature was less than 2 μbar/min, and were subsequently weighed to determine the mass of sample. Cyclohexane (dried over molecular sieves) was attached to the vapor-dosing manifold of the instrument, and frozen–pumped–thawed three times. In between each isotherm, the material was reactivated by heating the sample to 140 °C overnight or until the outgas rate at the degassing temperature was less than 2 μbar/min.

Isotherm Fitting. Adsorption isotherms for cyclohexane in Fe₂(dotpdc^R)·2DMF were fit with a single-site Langmuir–Freundlich equation (eq 2), where n is the total amount adsorbed in mmol/g, P is the pressure in bar, $n_{\text{sat},i}$ is the saturation capacity in mmol/g, b_i is the Langmuir parameter in bar⁻¹, and v_i is the Freundlich parameter.

$$n = \frac{n_{\text{sat},i} b_i P^{v_i}}{1 + b_i P^{v_i}} \quad (2)$$

Isosteric Heat of Adsorption Calculations. Using the Langmuir–Freundlich fits, the isosteric heat of adsorption, Q_{st} , can be calculated as a function of the total amount of gas adsorbed, n , by using the integrated form of the Clausius–Clapeyron equation (eq 3).

$$(\ln P)_n = \left(\frac{Q_{st}}{R} \right) \left(\frac{1}{T} \right) + C \quad (3)$$

For example, the cyclohexane Langmuir–Freundlich fits for $\text{Fe}_2(\text{dotpdc}) \cdot 2\text{DMF}$ were used to obtain the exact pressures that correspond to specific loadings at 25, 35, and 45 °C. This was done at loading intervals of 0.1 mmol/g. At each loading, the slope of $\ln(P)$ versus $1/T$ was calculated to obtain the isosteric heat.

RESULTS AND DISCUSSION

First studied in the context of O_2/N_2 separations, $\text{Fe}_2(\text{dobdc})$ (also known as Fe-MOF-74) is a functionally versatile metal–organic framework displaying exceptional performance in applications ranging from olefin/paraffin separations to gradual NO release for biomedical purposes.^{24,25} This versatility is due to the high density of coordinatively unsaturated iron(II) sites within the framework, which line the hexagonal pores and are both Lewis acidic and redox-active (see Figure 1). Recently, we discovered that $\text{Fe}_2(\text{dobdc})$ and its magnesium-diluted analogues also show promise as catalysts for hydrocarbon oxidation processes, converting ethane into ethanol and acetaldehyde in the presence of N_2O as a terminal oxidant.²⁶ Detailed computational studies support a high-spin, $S = 2$ iron(IV)–oxo intermediate,²⁷ which hydroxylates ethane via a radical rebound mechanism.²⁸

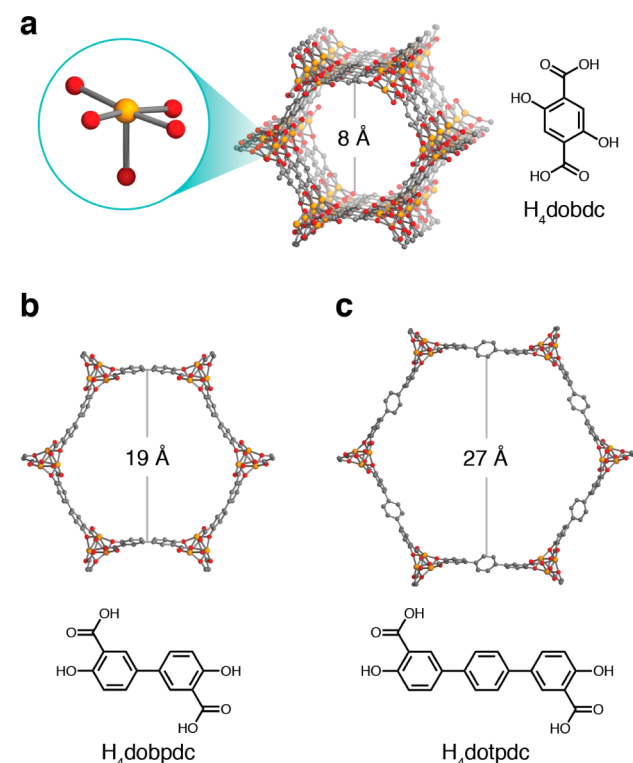


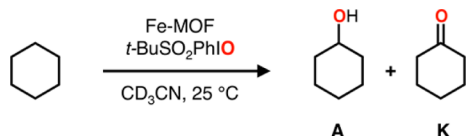
Figure 1. Portions of crystal structures of (a) $\text{Fe}_2(\text{dobdc})$, (b) $\text{Fe}_2(\text{dobpdc})$, and (c) $\text{Fe}_2(\text{dotpdc})$, and their corresponding ligands. (a) View of one-dimensional hexagonal pores of $\text{Fe}_2(\text{dobdc})$, with an inset showing the local coordination environment around each coordinatively unsaturated iron(II) site. The pore sizes indicated here were calculated from experimental 77 K N_2 adsorption isotherm data using DFT methods.

Our initial report emphasized the unusual primary coordination environment of the iron sites in $\text{Fe}_2(\text{dobdc})$, and its role in stabilizing the high-spin electronic structure of the iron–oxo unit. However, pore-expanded analogues of this material are also uniquely suited for exploring outer coordination sphere effects on metal site reactivity. First, framework interpenetration in this structure type is impossible, allowing the pore diameter to be increased at will. This concept was originally illustrated in the syntheses of mesoporous $\text{Mg}_2(\text{dobdc})$ analogues, with pore diameters ranging from 19 to 98 Å (denoted IRMOF-74-II through IRMOF-74-XI).²⁹ Furthermore, once the organic linker is expanded to three phenylene units and larger, a wide variety of organic substituents can be accommodated on the central rings without adversely affecting framework formation. The incorporation of such ligands directly during framework synthesis leads to pores coated with specifically chosen organic functionalities in crystallographically well-defined locations, whose properties (polarity, proticity, basicity) can be vastly different from the bulk reaction medium. The pore surface can also be chemically modified after synthesis, and postsynthetic incorporation of enzyme-like peptide chains has been recently demonstrated in IRMOF-74-III.³⁰ Leveraging these unique properties of the MOF-74 structure type, we sought to uncover the effect of pore diameter and chemical environment on the catalytic behavior of exposed iron sites in $\text{Fe}_2(\text{dobdc})$ and its related analogues.

Synthesis of Expanded $\text{Fe}_2(\text{dobdc})$ Derivatives. The two- and three-phenylene ring versions of $\text{Fe}_2(\text{dobdc})$, abbreviated $\text{Fe}_2(\text{dobpdc})$ ($\text{H}_4\text{dobpdc} = 4,4'$ -dihydroxy-[1,1'-biphenyl]-3,3'-dicarboxylic acid) and $\text{Fe}_2(\text{dotpdc})$ ($\text{H}_4\text{dotpdc} = 4,4''$ -dihydroxy-[1,1':4,1''-terphenyl]-3,3''-dicarboxylic acid), respectively, can be synthesized solvothermally to produce a series of frameworks possessing systematically increasing pore sizes of 8, 19, and 27 Å (see Figure 1). Note that these dimensions represent maxima in the pore size distributions calculated from 77 K N_2 adsorption isotherm data using density functional theory (DFT) methods, and are slightly less than the corresponding crystallographic pore diameters. The Brunauer–Emmett–Teller (BET) surface areas for $\text{Fe}_2(\text{dobdc})$, $\text{Fe}_2(\text{dobpdc})$, and $\text{Fe}_2(\text{dotpdc})$ are 1360, 2610, and 1970 m^2/g , respectively.^{24,31} The lower BET surface area of $\text{Fe}_2(\text{dotpdc})$ compared to $\text{Fe}_2(\text{dobpdc})$ is due to its significantly larger void volume, and is fully consistent with previously reported terphenyl frameworks of this structure type.²⁹ Note that, within a single hexagonal channel, the closest distance between iron sites lies down the c -axis and is independent of linker length (roughly 6.8–6.9 Å in all three frameworks). Therefore, this series primarily investigates the effect of an enlarged pore diameter, with other variables such as spatial separation of active sites and pore chemical environment held relatively constant.

Role of Pore Diameter in Cyclohexane Oxidation. In order to probe the effect of pore diameter on oxidation catalysis, solution-phase cyclohexane oxidation was investigated in $\text{Fe}_2(\text{dobdc})$, $\text{Fe}_2(\text{dobpdc})$, and $\text{Fe}_2(\text{dotpdc})$ as a representative reaction (see Scheme 1). The molecule $t\text{-BuSO}_2\text{PhIO}$, a soluble iodosylarene reagent commonly used to generate metal–oxo intermediates, was employed as the O atom transfer reagent and terminal oxidant in these reactions.³² Deuterated acetonitrile and an excess of cyclohexane were used to minimize possible solvent C–H activation side reactions.

Several important conclusions can be drawn from the results of cyclohexane oxidation in $\text{Fe}_2(\text{dobdc})$, $\text{Fe}_2(\text{dobpdc})$, and

Scheme 1. Oxidation of Cyclohexane to Cyclohexanol and Cyclohexanone in $\text{Fe}_2(\text{dobdc})$ and Expanded Pore Derivatives


$\text{Fe}_2(\text{dotpdc})$, as summarized in Table 1. First, only framework decomposition and leaching of Fe^{3+} cations was observed in the parent framework $\text{Fe}_2(\text{dobdc})$, with no detectable cyclohexane conversion. As a bulky oxidant with an approximate van der Waals volume of 221 \AA^3 ,³³ $t\text{-BuSO}_2\text{PhIO}$ likely cannot fit into the small channels of $\text{Fe}_2(\text{dobdc})$. This result provides evidence that the surface sites of $\text{Fe}_2(\text{dobdc})$, and most likely therefore those of the expanded analogues, are not catalytically active. Diffusion limitations of $t\text{-BuSO}_2\text{PhIO}$ and cyclohexane through the pores of $\text{Fe}_2(\text{dobpdc})$ may also explain why its turnover number (TON) is an order of magnitude lower than that of $\text{Fe}_2(\text{dotpdc})$ (0.3 versus 4). In contrast to the results obtained for $\text{Fe}_2(\text{dobdc})$, metal leaching was not observed for catalytic reactions conducted using the terphenyl derivative $\text{Fe}_2(\text{dotpdc})$ under these conditions. Furthermore, removal of the solid framework catalyst by filtration and subsequent addition of oxidant to the supernatant solution revealed no product formation occurs in the absence of $\text{Fe}_2(\text{dotpdc})$.

While gas-phase oxidation of ethane by $\text{Fe}_2(\text{dobdc})$ forms a complex mixture of overoxidized products and ether oligomers, presumably due to side reactions of a dissociated ethyl radical intermediate,^{26,34} $\text{Fe}_2(\text{dotpdc})$ generates cyclohexanol and cyclohexanone as the sole cyclohexane-derived oxidation products in high yield. For reasons that have yet to be conclusively determined, but may be related to the presence of an acetonitrile solvent cage,³⁵ the solution-phase cyclohexyl radical intermediate (and, in the case of cyclohexanone formation, the 1-cyclohexanonyl radical intermediate) appears much more well-behaved.

Finally, modest alcohol:ketone (A:K) ratios of 3.5:1 and 2.8:1 are observed for $\text{Fe}_2(\text{dobpdc})$ and $\text{Fe}_2(\text{dotpdc})$, respectively. These ratios reveal that significant oxidation of the product cyclohexanol to cyclohexanone occurs, despite the large excess of cyclohexane present under the reaction conditions. Because the formation of cyclohexanone likely proceeds by oxidation of initially formed cyclohexanol, these modest selectivities can be rationalized by considering the

Table 1. Summary of Cyclohexane Oxidation Results in Acetonitrile-Solvated $\text{Fe}_2(\text{dobdc})$, $\text{Fe}_2(\text{dobpdc})$, and $\text{Fe}_2(\text{dotpdc})$ ^a

framework	A:K ^b	yield (%) ^c (A + 2K)	TON ^d (A + 2K)
$\text{Fe}_2(\text{dobdc})$	N/A	N/A	N/A
$\text{Fe}_2(\text{dobpdc})$ ^e	3.5(1)	54(4)	0.3(1)
$\text{Fe}_2(\text{dotpdc})$	2.8(1)	76(6)	4(1)

^aGeneral conditions: 5.0 mg of acetonitrile-solvated framework, 25 mg of oxidant (0.073 mmol), 0.30 mL of cyclohexane (2.8 mmol), and 2.0 mL of CD_3CN . ^bRatio of cyclohexanol (A) to cyclohexanone (K). ^cMoles of product formed per mole of oxidant consumed. Note that cyclohexanone requires two oxidizing equivalents to form. ^dCatalytic turnovers, moles of product per mole of iron in catalyst. ^eTo obtain these results, 25 mg of framework was used; otherwise, significant framework decomposition and Fe leaching was observed.

preference of the framework interior, which is lined with Lewis acidic metal sites and carboxylate/aryloxy moieties, for polar adsorbates such as cyclohexanol. Thus, we sought to investigate whether this inherent bias could be suppressed through the introduction of nonpolar, hydrophobic groups to the framework walls.

Synthesis of Functionalized Terphenyl Derivatives $\text{Fe}_2(\text{dotpdc})$. To determine the effect of local hydrophobic groups on catalyst turnover number and selectivity, we synthesized three new derivatives of $\text{Fe}_2(\text{dotpdc})$ in which the central ring is replaced with tetrafluoro-, tetramethyl-, or 1,4-di-*tert*-butylaryl groups (see Figure 2 and Table 2). These three frameworks are abbreviated $\text{Fe}_2(\text{dotpdc}^{\text{R}})$ (R = F, CH_3 , and *t*Bu), respectively, with $\text{Fe}_2(\text{dotpdc})$ representing the completely unfunctionalized material. As a result of their location on the central phenylene ring, which is far removed from the iron(II) centers, these substituents should exert an influence on the overall pore chemical environment without directly interfering with the desired iron-oxo reactivity. Longer chain alkyl substituents were specifically avoided due to the possibility of ligand hydroxylation or other self-oxidation processes. Solvothermal synthesis conditions were used for all three frameworks, producing yellow, microcrystalline powders with diffraction patterns and unit cells consistent with the expanded $\text{M}_2(\text{dobdc})$ structure type (see Figures S1–S4 and Table S1). As the central substituents increase in size, the BET

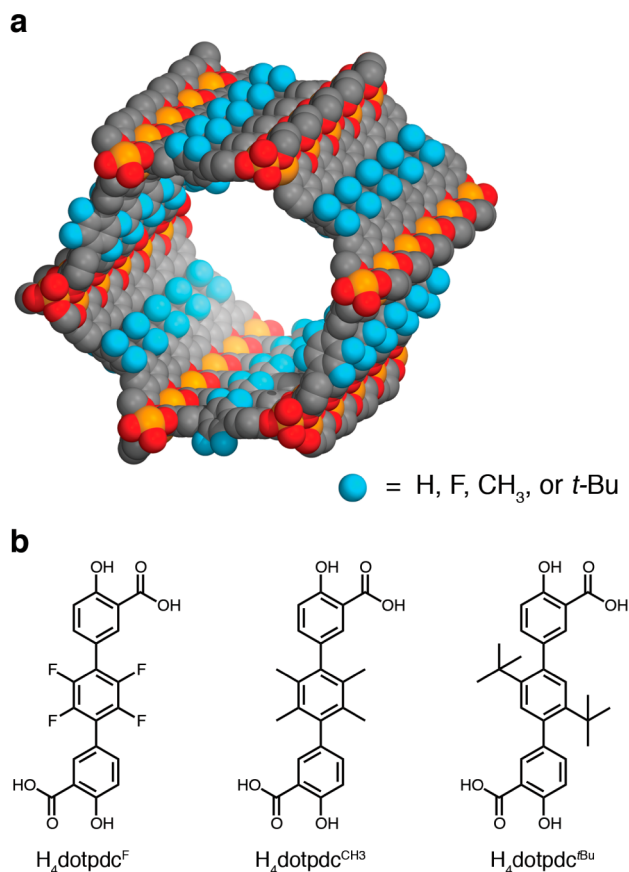


Figure 2. (a) View down the hexagonal channels of $\text{Fe}_2(\text{dotpdc}^{\text{R}})$, with substituents on the central phenylene ring highlighted in blue. (b) Structures of derivatized terphenyl linkers used in this work. The blue spheres represent H, F, CH_3 , or *t*Bu. Note that the *tert*-butyl derivative is only 1,4-disubstituted.

Table 2. Surface Areas and Pore Sizes of Fe₂(dotpdc) and Substituted Derivatives

framework	BET surf. area (m ² /g)	pore size ^a (Å)
Fe ₂ (dotpdc)	1970(30)	27
Fe ₂ (dotpdc ^F)	1880(20)	27
Fe ₂ (dotpdc ^{CH₃})	1860(50)	25
Fe ₂ (dotpdc ^{tBu})	1820(60)	24

^aDFT pore sizes calculated from 77 K N₂ adsorption isotherms.

surface areas and pore sizes correspondingly decrease (see Table 2). However, these differences are relatively minor, with only an ~10% reduction in surface area and pore size between Fe₂(dotpdc) and the most sterically crowded derivative, Fe₂(dotpdc^{tBu}). These results suggest that large reagents such as *t*-BuSO₂PhIO should still be able to diffuse freely through the functionalized triphenyl frameworks.

Influence of Hydrophobic Pore Environment on Cyclohexane Oxidation. While the surface areas, pore sizes, and unit cell parameters of the four Fe₂(dotpdc^R) frameworks are relatively similar, their cyclohexane oxidation A:K selectivities and turnover numbers are dramatically different, increasing in the order H < F < CH₃ < *t*Bu (see Table 3). Overall, a 3-fold increase in A:K ratio, from 2.8:1 to 8.4:1, and a 5-fold increase in TON, from 4 to 19, is apparent. In all cases, catalysis halts once the solid is removed from the reaction mixture, and no loss in framework crystallinity is evident (see Figure S6). While the ligand C–H bonds in Fe₂(dotpdc^{CH₃}) and Fe₂(dotpdc^{tBu}) could be susceptible to oxidative degradation, postcatalysis digestion and ¹H NMR analysis reveal no ligand oxidation (see Figures S7 and S8). The cause of catalyst deactivation appears to be the gradual oxidation of framework iron(II) sites to inactive iron(III) hydroxide or alkoxide moieties (confirmed by Mössbauer measurements), rather than framework collapse or ligand degradation. Iron(III) hydroxide species can form if initial H atom abstraction is followed by radical dissociation rather than rapid radical rebound.³⁴ In theory, it should be possible to regenerate the active Fe(II) catalyst through the use of an appropriate reductant.

Although the turnover numbers displayed by the Fe₂(dotpdc^R) family of frameworks are relatively modest, they do represent an improvement over similarly reactive non-heme iron(IV)–oxo molecular complexes, which can produce substoichiometric amounts of oxidized product due to radical

Table 3. Summary of Cyclohexane Oxidation Results in Acetonitrile-Solvated Fe₂(dobdc), Fe₂(dobpdc), and Fe₂(dotpdc)^a

framework	A:K ^b	yield (%) ^c (A + 2K)	TON ^d (A + 2K)
Fe ₂ (dotpdc)	2.8(1)	76(6)	4(1)
Fe ₂ (dotpdc ^F)	4.3(1)	84(7)	11(2)
Fe ₂ (dotpdc ^{CH₃})	6.5(1)	80(4)	13(2)
Fe ₂ (dotpdc ^{tBu})	8.4(4)	82(2)	19(1)

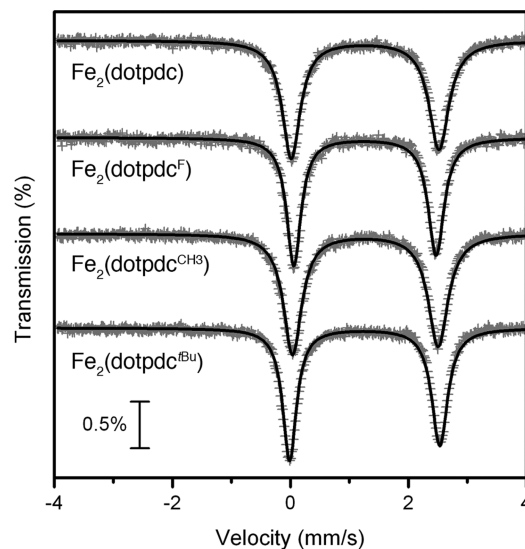
^aGeneral conditions: 5.0 mg of acetonitrile-solvated framework, 25 mg of oxidant (0.073 mmol), 0.30 mL of cyclohexane (2.8 mmol), and 2.0 mL of CD₃CN. ^bRatio of cyclohexanol (A) to cyclohexanone (K). ^cMoles of product formed per mole of oxidant consumed. Note that cyclohexanone requires two oxidizing equivalents to form. ^dCatalytic turnovers, moles of product per mole of iron in catalyst. Maximum TON was determined using 2.5 mg of framework and 25–75 mg of oxidant.

dissociation,^{34,36,37} bimolecular decomposition,³⁸ or ligand oxidation³⁹ pathways. However, it should be noted that there exist homogeneous, iron-based cyclohexane oxidation catalysts with TONs > 300,^{40,41} though the active oxidants in these systems are often free radicals and not metal–oxo intermediates. Similarly, while iron-based metal–organic frameworks such as Fe-MIL-101 and Fe(BTC) catalyze cyclohexane oxidation, these materials also operate via less selective radical chain mechanisms.⁴²

To determine whether the differing reactivity profiles displayed within the Fe₂(dotpdc^R) series are due to changes in ligand field strength arising from substituent inductive effects, Mössbauer spectroscopy was employed to probe the primary coordination sphere of the iron(II) sites. The spectra for the acetonitrile-solvated frameworks (see Figure 3) are remarkably similar across the series. In particular, the isomer shift (δ), a parameter that is highly sensitive to bonding properties such as bond length, metal–ligand covalency, and ligand electronegativity,⁴³ lies within the narrow range of 1.26–1.27 mm/s for all four frameworks (see Table S3). These results suggest ligand electronic effects and differences in the metal site primary coordination sphere are not responsible for the observed catalytic improvements.

Because the observed reactivity patterns could reflect subtle changes in the nature of the active intermediate or reaction mechanism, H/D kinetic isotope effects (KIEs) were used as a mechanistic probe of the putative iron(IV)–oxo intermediate. For heme and non-heme iron–oxo systems, combined theoretical and experimental efforts have shown that the H/D KIE is highly sensitive to variables such as transition state structure, spin state, and reaction barrier height.^{44–46} Notably, large KIE values of greater than 10, indicative of tunneling, are typically observed. For example, the non-heme iron enzyme TauD has a KIE of 37, while experimental values for high-spin iron(IV)–oxo model complexes range from 18 to 25.^{36b,47,48}

The cyclohexane oxidation H/D KIE values for the Fe₂(dotpdc^R) family were measured using in situ competition experiments between an excess of C₆H₁₂ and C₆D₁₂. The resulting values are 15.4(5), 14.4(2), 16.1(8), and 15.5(6), for

**Figure 3.** Mössbauer spectra of the four acetonitrile-solvated Fe₂(dotpdc^R) frameworks, collected at 100 K. Gray crosses and black lines represent raw data and corresponding fits, respectively.

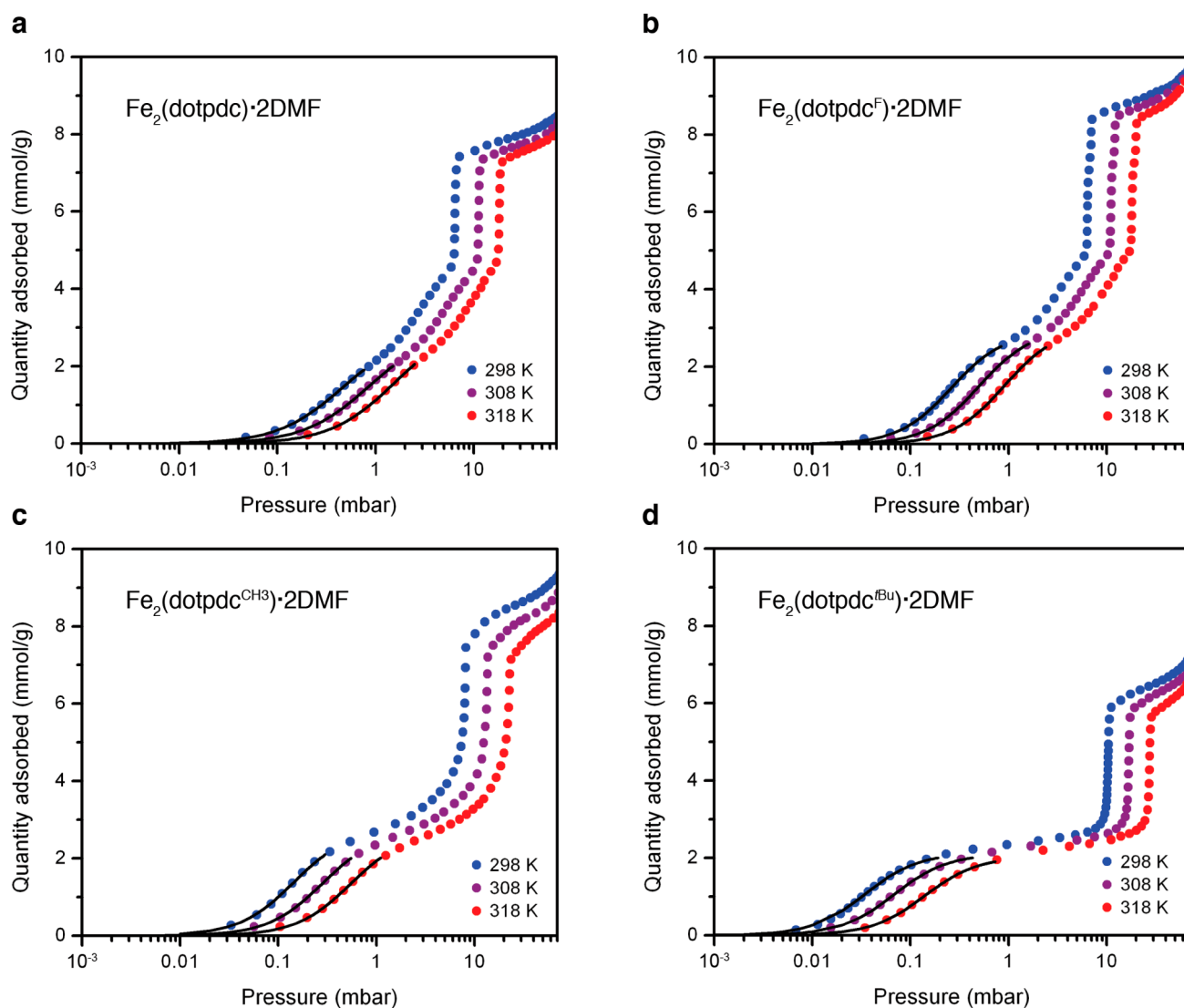


Figure 4. Cyclohexane gas adsorption isotherms for (a) $\text{Fe}_2(\text{dotpc})\cdot 2\text{DMF}$, (b) $\text{Fe}_2(\text{dotpc}^{\text{F}})\cdot 2\text{DMF}$, (c) $\text{Fe}_2(\text{dotpc}^{\text{CH}_3})\cdot 2\text{DMF}$, and (d) $\text{Fe}_2(\text{dotpc}^{\text{tBu}})\cdot 2\text{DMF}$. Blue, purple, and red circles represent experimental data collected at 298, 308, and 318 K, respectively; black lines are the corresponding single-site Langmuir–Freundlich fits to the data.

R = H, F, CH_3 , and *t*Bu, respectively (see Figure S9 and Table S4). All of these are above the semiclassical limit of 7, supporting the involvement of a metal–oxo species. Furthermore, the similarity of these values suggests that the observed reactivity differences are not due to changes in the iron–oxo intermediate.

Cyclohexane Adsorption in $\text{Fe}_2(\text{dotpc}^{\text{R}})$ Frameworks.

The Mössbauer and KIE experiments detailed above demonstrate that, at least within this series of frameworks, substitution of the remote central phenylene ring does not have a significant impact on the nature of either the iron(II) ground state or the iron(IV)–oxo intermediate. Therefore, we turned our attention away from primary coordination sphere properties and toward longer-range pore environment effects. Specifically, the adsorption of cyclohexane to the functionalized framework walls was examined. Liquid-phase adsorption experiments were first carried out using the catalytically relevant conditions of 1 M cyclohexane in acetonitrile. Interestingly, while the solution-phase cyclohexane capacity of $\text{Fe}_2(\text{dotpc})$ is around 2.0(3) mol/mol framework, the cyclohexane capacities of the substituted frameworks (R = F,

CH_3 , *t*Bu) are 1.7–2.1 times greater. Although these solution-phase studies do not provide detailed insight into specific framework–cyclohexane interactions, they do reveal that the $\text{Fe}_2(\text{dotpc}^{\text{R}})$ series of frameworks adsorb significant amounts of cyclohexane in the presence of acetonitrile.

To examine the thermodynamic properties of cyclohexane binding to the framework surface more closely, gas-phase cyclohexane isotherms for all four materials were collected in the pressure range of 0–100 mbar at three separate temperatures (see Figure 4). Note that the open iron(II) sites, which interact strongly with guest molecules, were capped with *N,N*-dimethylformamide (DMF) prior to data collection so that only physisorption to the framework walls was interrogated by these measurements. The cyclohexane isotherms for the four frameworks are qualitatively similar, with Langmuir behavior observed at low pressures and capillary condensation within the mesoporous channels occurring at higher pressures. The low-pressure region, corresponding to monolayer adsorption, was modeled with a single-site Langmuir–Freundlich equation (see Figure 4 and Table S5), and isosteric heats of adsorption (Q_{st}) were subsequently

calculated from these fits using the Clausius–Clapeyron equation (see Figure 5).

A cyclohexane isosteric heat of adsorption of $-45(1)$ kJ/mol was obtained for $\text{Fe}_2(\text{dotpdc})$, which is consistent with values previously reported for several metal–organic frameworks, faujasite-type zeolites, and carbon-based materials (-40 to -50 kJ/mol).^{49–52} While only a slightly stronger initial binding enthalpy of $-48(1)$ kJ/mol is seen in the tetrafluoro-substituted $\text{Fe}_2(\text{dotpdc}^{\text{F}})$, a large jump in adsorption enthalpy is observed once alkyl substituents are introduced to the organic linkers, with values of $-54(1)$ and $-57(1)$ kJ/mol obtained for $\text{Fe}_2(\text{dotpdc}^{\text{CH}_3})$ and $\text{Fe}_2(\text{dotpdc}^{\text{tBu}})$, respectively (see Figure 5). Importantly, the absolute values of these isosteric heats track precisely with the A:K selectivities observed for the cyclohexane oxidation reaction (Table 3). Coating the channel walls with hydrophobic moieties that interact favorably with cyclohexane may help funnel the substrate toward the iron center, increasing its local concentration relative to cyclohexanol and thereby improving the A:K selectivity. The cause of the dramatic increase in TON in $\text{Fe}_2(\text{dotpdc}^{\text{tBu}})$ is not yet clear, but may also be related to the more favorable adsorption of cyclohexane, as well as the confinement of radical intermediates close to the iron site by neighboring *tert*-butyl groups.

Structural models consistent with powder X-ray diffraction data provide further insight into the origin of the different cyclohexane adsorption behavior observed in these materials. In $\text{Fe}_2(\text{dotpdc})$, π – π stacking interactions between adjacent organic linkers generates a relatively flat, aromatic pore surface (see Figure 6 and Figure S5). In contrast, the increased steric bulk of the methyl and *tert*-butyl groups in $\text{Fe}_2(\text{dotpdc}^{\text{CH}_3})$ and $\text{Fe}_2(\text{dotpdc}^{\text{tBu}})$ leads to larger dihedral angles between the central phenylene unit and its neighboring rings. In $\text{Fe}_2(\text{dotpdc}^{\text{tBu}})$, the large *tert*-butyl substituents extend directly into the channels, lining the pore wall with hydrophobic residues and providing additional van der Waals interactions for cyclohexane binding. Interestingly, these models suggest the local environment around the iron site in $\text{Fe}_2(\text{dotpdc}^{\text{tBu}})$ is significantly more sterically congested than in $\text{Fe}_2(\text{dotpdc})$, which may help maintain the cyclohexane molecule and

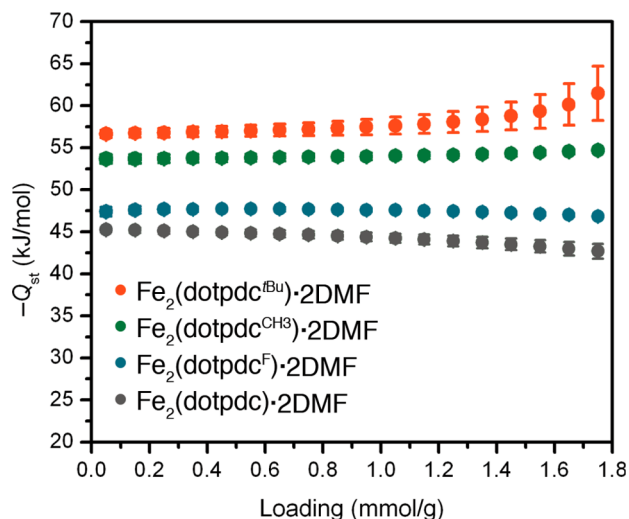


Figure 5. Cyclohexane isosteric heats of adsorption (Q_{st}) for $\text{Fe}_2(\text{dotpdc})$ (gray), $\text{Fe}_2(\text{dotpdc}^{\text{F}})$ (turquoise), $\text{Fe}_2(\text{dotpdc}^{\text{CH}_3})$ (green), and $\text{Fe}_2(\text{dotpdc}^{\text{tBu}})$ (orange).

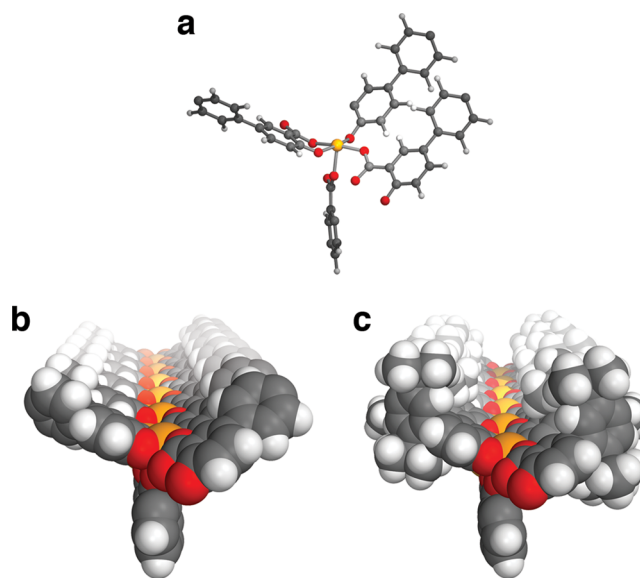


Figure 6. Local structure of the iron(II) centers in $\text{Fe}_2(\text{dotpdc})$ and $\text{Fe}_2(\text{dotpdc}^{\text{tBu}})$. (a) Ball-and-stick model of the iron(II) center in $\text{Fe}_2(\text{dotpdc})$ and (b) its corresponding space-filling model, as viewed down a channel. (c) Space-filling model of the iron(II) centers as viewed down a channel in $\text{Fe}_2(\text{dotpdc}^{\text{tBu}})$. White, gray, red, and orange spheres represent H, C, O, and Fe, respectively.

cyclohexyl radical near the iron center as the reaction progresses.

CONCLUSIONS AND OUTLOOK

Specifically engineered host–guest interactions in metal–organic frameworks, which have been previously utilized for gas separation and storage purposes, are a powerful parameter in catalyst design. Functionalization of remote framework sites can lead to large changes in substrate adsorption and binding patterns that can in turn strongly alter the course of a catalytic reaction. Here, incorporation of simple nonpolar groups remarkably increases both the selectivity and stability of framework-embedded iron sites for cyclohexane oxidation catalysis without directly affecting the structure or reactivity of the iron centers themselves. Outer coordination sphere and pore environment effects may prove to be significant in the context of many other metal–organic framework-catalyzed reactions, and are well worthy of further investigation.

ASSOCIATED CONTENT

Supporting Information

The Supporting Information is available free of charge on the ACS Publications website at DOI: 10.1021/jacs.6b08417.

Additional experimental details, including control experiments, framework digestion protocols, ligand syntheses, gas sorption, powder diffraction, and Mössbauer data (PDF)

AUTHOR INFORMATION

Corresponding Author

*jrlong@berkeley.edu

Notes

The authors declare no competing financial interest.

ACKNOWLEDGMENTS

The synthetic chemistry, structural analysis, and characterization of gas adsorption properties were supported through the Center for Gas Separations Relevant to Clean Energy Technologies, an Energy Frontier Research Center funded by the U.S. Department of Energy, Office of Science, Office of Basic Energy Sciences, under Award DE-SC0001015. The reactivity studies were supported by the Nanoporous Materials Genome Center, funded by the U.S. Department of Energy, Office of Basic Energy Sciences, Division of Chemical Sciences, Geosciences and Biosciences, under Award DE-FG02-12ER16362. This research also used resources of the Advanced Photon Source, a U.S. Department of Energy (DOE) Office of Science User Facility operated for the DOE Office of Science by Argonne National Laboratory under Contract No. DE-AC02-06CH11357. We thank Douglas A. Reed, Miguel I. Gonzalez, and David Z. Zee for experimental assistance and helpful discussions.

REFERENCES

- (1) (a) Zhao, M.; Wang, H.-B.; Ji, L.-N.; Mao, Z.-W. *Chem. Soc. Rev.* **2013**, *42*, 8360–8375. (b) Raynal, M.; Ballester, P.; Vidal-Ferran, A.; van Leeuwen, P. W. N. M. *Chem. Soc. Rev.* **2014**, *43*, 1734–1787. (c) Cook, S. A.; Borovik, A. S. *Acc. Chem. Res.* **2015**, *48*, 2407–2414.
- (2) Borovik, A. S. *Acc. Chem. Res.* **2005**, *38*, 54–61.
- (3) (a) Murakami, Y.; Kikuchi, J.-I.; Hisaeda, Y.; Hayashida, O. *Chem. Rev.* **1996**, *96*, 721–758. (b) Breslow, R.; Dong, S. D. *Chem. Rev.* **1998**, *98*, 1997–2012. (c) Homden, D. M.; Redshaw, C. *Chem. Rev.* **2008**, *108*, 5086–5130.
- (4) Fiedler, D.; Leung, D. H.; Bergman, R. G.; Raymond, K. N. *Acc. Chem. Res.* **2005**, *38*, 349–358.
- (5) Derouane, E. G. *J. Mol. Catal. A: Chem.* **1998**, *134*, 29–45.
- (6) Doyle, A. G.; Jacobsen, E. N. *Chem. Rev.* **2007**, *107*, 5713–5743.
- (7) Shook, R. L.; Borovik, A. S. *Inorg. Chem.* **2010**, *49*, 3646–3660.
- (8) Rakowski Dubois, M.; DuBois, D. L. *Chem. Soc. Rev.* **2009**, *38*, 62–72.
- (9) Costentin, C.; Robert, M.; Savéant, J.-M. *Chem. Soc. Rev.* **2013**, *42*, 2423–2436.
- (10) Primo, A.; Garcia, H. *Chem. Soc. Rev.* **2014**, *43*, 7548–7561.
- (11) Dyson, P. J.; Jessop, P. G. *Catal. Sci. Technol.* **2016**, *6*, 3302–3316.
- (12) Weitkamp, J.; Ernst, S.; Puppe, L. Shape-Selective Catalysis in Zeolites. In *Catalysis and Zeolites: Fundamentals and Applications*; Weitkamp, J., Puppe, L., Eds.; Springer: New York, 1999; pp 327–376.
- (13) Corma, A. *J. Catal.* **2003**, *216*, 298–312.
- (14) Corma, A. *Chem. Rev.* **1997**, *97*, 2373–2420.
- (15) (a) Wight, A. P.; Davis, M. E. *Chem. Rev.* **2002**, *102*, 3589–3614. (b) Taguchi, A.; Schüth, F. *Microporous Mesoporous Mater.* **2005**, *77*, 1–45.
- (16) (a) Chen, B.; Xiang, S.; Qian, G. *Acc. Chem. Res.* **2010**, *43*, 1115–1124. (b) Li, J.-R.; Sculley, J.; Zhou, H.-C. *Chem. Rev.* **2012**, *112*, 869–932.
- (17) (a) Deng, H.; Doonan, C. J.; Furukawa, H.; Ferreira, R. B.; Towne, J.; Knobler, C. B.; Wang, B.; Yaghi, O. M. *Science* **2010**, *327*, 846–850. (b) Kong, X.; Deng, H.; Yan, F.; Kim, J.; Swisher, J. A.; Smit, B.; Yaghi, O. M.; Reimer, J. A. *Science* **2013**, *341*, 882–885. (c) Liu, L.; Konstantas, K.; Hill, M. R.; Telfer, S. G. *J. Am. Chem. Soc.* **2013**, *135*, 17731–17734. (d) Yuan, S.; Chen, Y.-P.; Qin, J.-S.; Lu, W.; Zou, L.; Zhang, Q.; Wang, X.; Sun, X.; Zhou, H.-C. *J. Am. Chem. Soc.* **2016**, *138*, 8912–8919.
- (18) (a) Lee, J.; Farha, O. K.; Roberts, J.; Scheidt, K. A.; Nguyen, S. T.; Hupp, J. T. *Chem. Soc. Rev.* **2009**, *38*, 1450–1459. (b) Ma, L.; Abney, C.; Lin, W. *Chem. Soc. Rev.* **2009**, *38*, 1248–1256. (c) Liu, J.; Chen, L.; Cui, H.; Zhang, J.; Zhang, L.; Su, C.-Y. *Chem. Soc. Rev.* **2014**, *43*, 6011–6061. (d) Cohen, S. M.; Zhang, Z.; Boissonnault, J. A. *Inorg. Chem.* **2016**, *55*, 7281–7290.
- (19) (a) Song, F.; Wang, C.; Falkowski, J. M.; Ma, L.; Lin, W. *J. Am. Chem. Soc.* **2010**, *132*, 15390–15398. (b) Roberts, J. M.; Fini, B. M.; Sarjeant, A. A.; Farha, O. K.; Hupp, J. T.; Scheidt, K. A. *J. Am. Chem. Soc.* **2012**, *134*, 3334–3337. (c) Lu, G.; Li, S.; Guo, Z.; Farha, O. K.; Hauser, B. G.; Qi, X.; Wang, Y.; Wang, X.; Han, S.; Liu, X.; DuChene, J. S.; Zhang, H.; Zhang, Q.; Chen, X.; Ma, J.; Loo, S. C. J.; Wei, W. D.; Yang, Y.; Hupp, J. T.; Huo, F. *Nat. Chem.* **2012**, *4*, 310–316. (d) Metzger, E. D.; Brozek, C. K.; Comito, R. J.; Dincă, M. *ACS Cent. Sci.* **2016**, *2*, 148–153.
- (20) (a) Bloch, W. M.; Burgun, A.; Coghlan, C. J.; Lee, R.; Coote, M. L.; Doonan, C. J.; Sumbly, C. J. *Nat. Chem.* **2014**, *6*, 906–912. (b) Gonzalez, M. I.; Bloch, E. D.; Mason, J. A.; Teat, S. J.; Long, J. R. *Inorg. Chem.* **2015**, *54*, 2995–3005.
- (21) (a) *Cytochrome P450: Structure, Mechanism, and Biochemistry*; Ortiz de Montellano, P. R., Ed.; Kluwer Academic/Plenum Publishers: New York, 2005. (b) Costas, M.; Mehn, M. P.; Jensen, M. P.; Que, L., Jr. *Chem. Rev.* **2004**, *104*, 939–986.
- (22) Feiters, M. C.; Rowan, A. E.; Nolte, R. J. M. *Chem. Soc. Rev.* **2000**, *29*, 375–384.
- (23) Bhadra, B. N.; Cho, K. H.; Khan, N. A.; Hong, D.-Y.; Jhung, S. H. *J. Phys. Chem. C* **2015**, *119*, 26620–26627.
- (24) Bloch, E. D.; Murray, L. J.; Queen, W. L.; Chavan, S.; Maximoff, S. N.; Bigi, J. P.; Krishna, R.; Peterson, V. K.; Grandjean, F.; Long, G. J.; Smit, B.; Bordiga, S.; Brown, C. M.; Long, J. R. *J. Am. Chem. Soc.* **2011**, *133*, 14814–14822.
- (25) (a) Bloch, E. D.; Queen, W. L.; Krishna, R.; Zadrozny, J. M.; Brown, C. M.; Long, J. R. *Science* **2012**, *335*, 1606–1610. (b) Bloch, E. D.; Hudson, M. R.; Mason, J. A.; Chavan, S.; Crocellà, V.; Howe, J. D.; Lee, K.; Dzubak, A. L.; Queen, W. L.; Zadrozny, J. M.; Geier, S. J.; Lin, L.-C.; Gagliardi, L.; Smit, B.; Neaton, J. B.; Bordiga, S.; Brown, C. M.; Long, J. R. *J. Am. Chem. Soc.* **2014**, *136*, 10752–10761. (c) Bloch, E. D.; Queen, W. L.; Chavan, S.; Wheatley, P. S.; Zadrozny, J. M.; Morris, R.; Brown, C. M.; Lamberti, C.; Bordiga, S.; Long, J. R. *J. Am. Chem. Soc.* **2015**, *137*, 3466–3469.
- (26) Xiao, D. J.; Bloch, E. D.; Mason, J. A.; Queen, W. L.; Hudson, M. R.; Planas, N.; Borycz, J.; Dzubak, A. L.; Verma, P.; Lee, K.; Bonino, F.; Crocellà, V.; Yano, J.; Bordiga, S.; Truhlar, D. G.; Gagliardi, L.; Brown, C. M.; Long, J. R. *Nat. Chem.* **2014**, *6*, 590–595.
- (27) Puri, M.; Que, L., Jr. *Acc. Chem. Res.* **2015**, *48*, 2443–2452.
- (28) Verma, P.; Vogiatzis, K. D.; Planas, N.; Borycz, J.; Xiao, D. J.; Long, J. R.; Gagliardi, L.; Truhlar, D. G. *J. Am. Chem. Soc.* **2015**, *137*, 5770–5781.
- (29) Deng, H.; Grunder, S.; Cordova, K. E.; Valente, C.; Furukawa, H.; Hmadeh, M.; Gándara, F.; Whalley, A. C.; Liu, Z.; Asahina, S.; Kazumori, H.; O’Keeffe, M.; Terasaki, O.; Stoddart, J. F.; Yaghi, O. M. *Science* **2012**, *336*, 1018–1023.
- (30) Fracaro, A. M.; Siman, P.; Nagib, D. A.; Suzuki, M.; Furukawa, H.; Toste, F. D.; Yaghi, O. M. *J. Am. Chem. Soc.* **2016**, *138*, 8352–8355.
- (31) (a) McDonald, T. M.; Mason, J. A.; Kong, X.; Bloch, E. D.; Gygi, D.; Dani, A.; Crocella, V.; Giordanino, F.; Odoh, S. O.; Drisdell, W. S.; Vlaisavljevich, B.; Dzubak, A. L.; Poloni, R.; Schnell, S. K.; Planas, N.; Lee, K.; Pascal, T.; Wan, L. F.; Prendergast, D.; Neaton, J. B.; Smit, B.; Kortright, J. B.; Gagliardi, L.; Bordiga, S.; Reimer, J. A.; Long, J. R. *Nature* **2015**, *519*, 303–308. (b) Gygi, D.; Bloch, E. D.; Mason, J. A.; Hudson, M. R.; Gonzalez, M. I.; Siegelman, R. L.; Darwish, T. A.; Queen, W. L.; Brown, C. M.; Long, J. R. *Chem. Mater.* **2016**, *28*, 1128–1138.
- (32) Under the conditions we investigated, we found that N₂O, when used in combination with liquid-phase hydrocarbons, leads to no observable reaction due to its poor metal-binding properties and sluggish oxidation kinetics.
- (33) Zhao, Y. H.; Abraham, M. H.; Zissimos, A. M. *J. Org. Chem.* **2003**, *68*, 7368–7373.
- (34) Cho, K.-B.; Hirao, H.; Shaik, S.; Nam, W. *Chem. Soc. Rev.* **2016**, *45*, 1197–1210.
- (35) Lorand, J. P. In *Progress in Inorganic Chemistry: Inorganic Reaction Mechanisms: Part II*; Edwards, J. O., Ed.; John Wiley & Sons, Inc.: Hoboken, NJ, 1972; Vol. 17, pp 207–325.

(36) (a) Kaizer, J.; Klinker, E. J.; Oh, N. Y.; Rohde, J.-U.; Song, W. J.; Stubna, A.; Kim, J.; Münck, E.; Nam, W.; Que, L., Jr. *J. Am. Chem. Soc.* **2004**, *126*, 472–473. (b) Biswas, A. N.; Puri, M.; Meier, K. K.; Oloo, W. N.; Rohde, G. T.; Bominaar, E. L.; Münck, E.; Que, L., Jr. *J. Am. Chem. Soc.* **2015**, *137*, 2428–2431.

(37) (a) Cho, K.-B.; Wu, X.; Lee, Y.-M.; Kwon, Y. H.; Shaik, S.; Nam, W. *J. Am. Chem. Soc.* **2012**, *134*, 20222–20225. (b) Bae, S. H.; Seo, M. S.; Lee, Y.-M.; Cho, K.-B.; Kim, W.-S.; Nam, W. *Angew. Chem., Int. Ed.* **2016**, *55*, 8027–8031.

(38) (a) Que, L., Jr. *Acc. Chem. Res.* **2007**, *40*, 493–500. (b) Vermeulen, N. A.; Chen, M. S.; White, M. C. *Tetrahedron* **2009**, *65*, 3078–3084.

(39) England, J.; Guo, Y.; Farquhar, E. R.; Young, V. G., Jr.; Münck, E.; Que, L., Jr. *J. Am. Chem. Soc.* **2010**, *132*, 8635–8644.

(40) (a) Talsi, E. P.; Bryliakov, K. P. *Coord. Chem. Rev.* **2012**, *256*, 1418–1434. (b) Lindhorst, A. C.; Haslinger, S.; Kühn, F. E. *Chem. Commun.* **2015**, *51*, 17193–17212.

(41) Fernandes, R. R.; Kirillova, M.; da Silva, J. A. L.; Fraústo da Silva, J. J. R.; Pombeiro, A. J. L. *Appl. Catal., A* **2009**, *353*, 107–112. (b) Silva, T. F. S.; da Silva, M. F. G.; Mishra, G. S.; Martins, L. M. D. R. S.; Pombeiro, A. M. L. *J. Organomet. Chem.* **2011**, *696*, 1310–1318.

(42) (a) Dhakshinamoorthy, A.; Alvaro, M.; Garcia, H. *Chem. - Eur. J.* **2011**, *17*, 6256–6262. (b) Maksimchuk, N. V.; Kovalenko, K. A.; Fedin, V. P.; Kholdeeva, O. A. *Chem. Commun.* **2012**, *48*, 6812–6814. (c) Mikami, Y.; Dhakshinamoorthy, A.; Alvaro, M.; Garcia, H. *ChemCatChem* **2013**, *5*, 1964–1970. (d) Cele, M. N.; Friedrich, H. B.; Bala, M. D. *Catal. Commun.* **2014**, *57*, 99–102.

(43) Gütlich, P.; Bill, E.; Trautwein, A. Hyperfine Interactions. In *Mössbauer Spectroscopy and Transition Metal Chemistry: Fundamentals and Applications*; Springer: New York, 2011; pp 73–135.

(44) Li, C.; Wu, W.; Kumar, D.; Shaik, S. *J. Am. Chem. Soc.* **2006**, *128*, 394–395.

(45) Klinker, E. J.; Shaik, S.; Hirao, H.; Que, L., Jr. *Angew. Chem., Int. Ed.* **2009**, *48*, 1291–1295.

(46) Shaik, S.; Hirao, H.; Kumar, D. *Acc. Chem. Res.* **2007**, *40*, 532–542.

(47) Price, J. C.; Barr, E. W.; Glass, T. E.; Krebs, C.; Bollinger, J. M., Jr. *J. Am. Chem. Soc.* **2003**, *125*, 13008–13009.

(48) England, J.; Martinho, M.; Farquhar, E. R.; Frisch, J. R.; Bominaar, E. L.; Münck, E.; Que, L., Jr. *Angew. Chem., Int. Ed.* **2009**, *48*, 3622–3626.

(49) Finsky, V.; Calero, S.; García-Pérez, E.; Merklings, P. J.; Vedts, G.; De Vos, D. E.; Baron, G. V.; Denayer, J. F. M. *Phys. Chem. Chem. Phys.* **2009**, *11*, 3515–3521.

(50) Lee, J. Y.; Olson, D. H.; Pan, L.; Emge, T. J.; Li, J. *Adv. Funct. Mater.* **2007**, *17*, 1255–1262.

(51) Dzhigit, O. M.; Kiselev, A. V.; Rachmanova, T. A. *Zeolites* **1984**, *4*, 389–397.

(52) Díaz, E.; Ordóñez, S.; Vega, A. J. *Colloid Interface Sci.* **2007**, *305*, 7–16.